

Fast charge storage kinetics by surface engineering for Ni-rich layered oxide cathodes

Jiacheng Wang, Zhenyu Zhang, Weitao He, Zhixuan Wang, Suting Weng, Quan Li, Xuefeng Wang, Suelen Barg, Liquan Chen, Hong Li, Fan Wu

Angaben zur Veröffentlichung / Publication details:

Wang, Jiacheng, Zhenyu Zhang, Weitao He, Zhixuan Wang, Suting Weng, Quan Li, Xuefeng Wang, et al. 2023. "Fast charge storage kinetics by surface engineering for Ni-rich layered oxide cathodes." Journal of Materials Chemistry A 11 (19): 10239–53. <https://doi.org/10.1039/d3ta00890h>.

Fast charge storage kinetics by surface engineering for Ni-rich layered oxide cathodes†

Jiacheng Wang,^a Zhenyu Zhang,^f Weitao He,^a Zhixuan Wang,^{acd} Suting Weng,^d Quan Li,^g Xuefeng Wang,^{ad} Suelen Barg,^{hi} Liquan Chen,^{abcd} Hong Li^{abcdefg} and Fan Wu^{abcde}

A Ni-rich (Ni content $\geq 80\%$) layered oxide (NRLO) cathode is a promising candidate for boosting the energy density of Li-ion batteries due to its high discharge voltage and capacities over 200 mA h g^{-1} . However, hindrance to Li transport due to limited Li-vacant sites, NiO-like rock-salt structures and resistant surface Li residuals restricts its practical electrochemical performances. Herein, controlled water treatment was applied to modify the surface crystal structure and chemical environment of $\text{LiNi}_{0.83}\text{Co}_{0.11}\text{Mn}_{0.06}\text{O}_2$ (NCM83), which improved Li transport kinetics within NCM83 lattices and across cathode/electrolyte interfaces. Li–H₂O interactions during water treatment caused chemical de-lithiation at the NCM83 surface and induced Li migration from the bulk to the surface of NCM83, facilitating the construction of Li-vacant layered structures at the NCM83 surface after a heat treatment in an oxygen-rich environment. dQ/dV vs. V curves revealed that surface Li vacancies promoted Li migrations in the NCM83 lattice at a low state of charge (SOC), improving the reversibility of the H1 phase transformation of NCM83 and hence boosting the reversible capacity. Additionally, the concurrent removal of Li residuals on the NCM83 surface by water treatment also ameliorated Li transport across cathode/electrolyte interfaces and prevented side reactions induced by Li_2CO_3 decomposition, enhancing the rate performance and cycling stability of NCM83. NCM83 with Li-vacant surface layered structures and the lowest Li residual content displayed a high 1st cycle reversible capacity of $212.8 \text{ mA h g}^{-1}$ (coulombic efficiency of 94.9%) and capacity retention of 89.4% over 100 cycles.

1 Introduction

Ni-rich (Ni content $\geq 80\%$) layered oxide (NRLO) cathode materials are known for their high capacities and low cost,

which make them promising candidates for boosting the driving range of electric automobiles.^{1–4} As the Ni content increases, the open-circuit voltage at a given Li concentration of NRLO decreases, which means high capacities can be achieved over a narrow voltage range.^{5,6} However, unstable Ni^{3+} ions lead to narrow stability windows of NRLOs. The reduction of Ni^{3+} ions to Ni^{2+} causes Li/Ni mixing due to the similar ionic radii of Ni^{2+} (0.69 Å) and Li^+ (0.76 Å),⁷ which triggers structural reconstruction from layered to rock-salt phases.⁸ Ni ions in Li layers reduce the interlayer spacing and act as pillars, which impedes Li migration within the NRLO lattice and degrades the kinetics of electrochemical reactions.^{9,10} To minimize Li/Ni mixing and compensate for Li loss during NRLO synthesis, extra Li precursors are used, which leads to the formation of Li residual compounds such as Li_2O , LiOH and Li_2CO_3 on the NRLO surface. These Li residual compounds have low electronic and ionic conductivities, leading to increased charge transfer resistance at the cathode/electrolyte interface. Moreover, Li_2CO_3 decomposes at high voltages into CO_2 and active singlet $^1\text{O}_2$ to induce electrolyte decompositions and growth of cathode/electrolyte interface (CEI) layers, further reducing the charge transfer kinetics.^{11,12} In addition, H₂O in air induces chemical delithiation of NRLOs and formation of more Li residual

^aTianmu Lake Institute of Advanced Energy Storage Technologies, Liyang 213300, Jiangsu, China

^bYangtze River Delta Physics Research Center, Liyang 213300, Jiangsu, China

^cBeijing Advanced Innovation Center for Materials Genome Engineering, Key Laboratory for Renewable Energy, Beijing Key Laboratory for New Energy Materials and Devices, Institute of Physics, Chinese Academy of Sciences, Beijing, 100190, China. E-mail: fwu@iphy.ac.cn

^dSchool of Physical Sciences, University of Chinese Academy of Sciences, Beijing, 100049, China

^eNano Science and Technology Institute, University of Science and Technology of China, Suzhou 215123, China

^fBeijing WeLion New Energy Technology Co., Ltd, Beijing, 102402, China

^gHuairou Division, Institute of Physics, Chinese Academy of Sciences, Beijing, 101400, China

^hHenry Royce Institute and Department of Materials, School of Natural Sciences, The University of Manchester, Manchester, M13 9PL, UK

ⁱInstitute of Materials Resource Management (MRM), Augsburg University, Am Technologiezentrum 8, 86159, Augsburg, Germany

† Electronic supplementary information (ESI) available. See DOI: <https://doi.org/10.1039/d3ta00890h>

compounds in an ambient environment.^{13–18} Studies show that the formation of Li residuals during ambient storage is accompanied by the reduction of Ni³⁺ to Ni²⁺ which potentially leads to the formation of rock salt phases at the NRLO surface, impeding Li diffusion and degrading electrochemical performance of NRLOs.^{17–20}

Another crucial factor determining the kinetics of electrochemical reactions is the diffusion of Li ions within an NRLO lattice. It has been proposed that Li ions migrate in NRLOs following a tetrahedral site hopping (TSH) mechanism where the migrating Li ion jumps from one octahedral site to another vacant octahedral site *via* an intermediate tetrahedral site.^{8,21} High migration barriers to Li diffusion at low SOC (~ 3.4 – 3.7 V *vs.* Li/Li⁺) are caused by the absence of Li divacancies and high electrostatic repulsions.^{21,22} The hindered Li diffusion in turn results in suppressed H1 phase transformations and increased irreversible capacities.^{21,22} On the other hand, the reversibility of H1 phase transformation can be enhanced when Li-deficient phases are formed after the 1st charge/discharge cycle due to increased Li vacancy concentrations and expanded interlayer spacing, which facilitates Li diffusion.²⁵ At high SOC (4.1–4.3 V *vs.* Li/Li⁺), Li diffusion rate degrades due to contraction of interlayer spacing and increased valence states of transition metals as the space of the intermediate tetrahedral site is reduced and the electrostatic repulsion between migrating Li ions and neighbouring cations is increased.⁸ Therefore, H3 phase transformation of NRLOs at high SOC is also inhibited by hindered Li diffusion. Moreover, slow Li diffusion creates a Li concentration gradient within the NRLO lattice and hence, variations in lattice parameters, which in turn causes internal lattice stress and micro-crack formation in NRLO particles.²⁶ Electrochemical reactions at low and high SOC are further suppressed due to cracking of NRLOs, which is a major reason for capacity fading over cycling.²⁷

Li residuals at the NRLO surface have been removed by washing with water, ethanol²⁸ and acid²⁹. While water is more effective in dissolving Li₂O, LiOH and Li₂CO₃, it has been shown to extract Li ions from the NRLO lattice due to Li–H exchange, creating highly resistive NiO-like surface layers which substantially increase the interfacial impedance and deteriorate battery performances.^{30–32} Other studies have shown improved electrochemical performance after water exposure.^{33,34} However, Li residuals are not sufficiently removed, or advantageous surface structure reconstruction is not achieved by their methods.

Herein, LiNi_{0.83}Co_{0.11}Mn_{0.06}O₂ (NCM83) was subjected to controlled water washing treatment. By minimizing the washing time and controlling the water/NCM83 ratio, Li-vacant surface layered structures were constructed and the Li residual content was reduced, leading to improved electrochemical performances of NCM83. Analysis of dQ/dV *vs.* V curves revealed that the reversibility of the H1 phase transformation was apparently enhanced after water washing, which significantly increased the 1st cycle reversible capacity. Detailed characterization corroborated that Li–H₂O interactions during water treatment followed by heat treatment in an oxygen-rich environment lead to the formation of Li-vacant layered structures at the NCM83 surface, which facilitated Li migration in the

NCM83 lattice at low SOC and hence enhanced the reversibility of H1 phase transformations. Moreover, removal of Li residuals improved Li ion transport across the cathode/electrolyte interface and prevented side reactions caused by Li₂CO₃ decomposition, leading to enhanced rate performance and cycling stability of NCM83.

2 Results and discussion

Pristine NCM83s (NCM-S0) were subjected to water-washing and humid-air exposure treatments in this study. NCM83s that went through water-washing treatment with NCM83 : water ratios of 1 : 0.5, 1 : 1.5 and 1 : 2 are denoted as NCM-W1, NCM-W2 and NCM-W3, respectively, while those exposed to 77%-humidity air for 1.5 and 18 hours are denoted as NCM-A1 and NCM-A2, respectively. The concentration of Li residuals for different NCM83s was measured using HCl titration as shown in Table 1. The concentrations of LiOH and Li₂CO₃ were derived from measured contents of OH[−] and CO₃^{2−} groups in the titrant. It should be noted that LiOH may originally exist on the NCM83 surface or come from Li₂O after its reaction with water. The initial LiOH and Li₂CO₃ contents for NCM-S0 are 0.53 and 0.55 wt%, respectively. As the NCM83 : water ratio decreases, the concentrations of LiOH and Li₂CO₃ decrease, indicating that more LiOH/Li₂O and Li₂CO₃ were removed as the water content increased. In contrast, humid-air-exposed samples show a decreased concentration of LiOH and increased concentration of Li₂CO₃, indicating that LiOH/Li₂O reacted with CO₂ in air to form Li₂CO₃. The total Li residual content increases after humid-air exposure, indicating that H₂O–NCM83 interactions induce chemical delithiation and formation of more Li residual compounds. The relatively lower contents of Li₂CO₃ and total Li residuals for NCM-A2 compared to those for NCM-A1 are due to the change in environmental temperature during the measurement.

XRD patterns of different NCM83s reveal a typical α -NaFeO₂-type structure without observable impurity signals (Fig. 1a). The splitting of (108)–(110) peaks is an indication of layered structures as those peaks merge in rock-salt phases.³⁵ The closer-up image (Fig. 1b) shows clear splitting of (108)–(110) peaks for all samples. The separation between (108) and (110) peaks ($\Delta\theta$) is sensitive to the degree of chemical delithiation of LiNiO₂ as shown by ref. 36 and follows a linear relationship with the ratio between lattice parameters *c* and *a* (*c/a*).³⁷ For a hexagonal

Table 1 Li residual contents of different NCM83s measured by pH titration

NCM83	LiOH wt%	Li ₂ CO ₃ wt%	Total Li residuals wt%
NCM-W3	0.16	0.12	0.28
NCM-W2	0.22	0.15	0.37
NCM-W1	0.21	0.33	0.54
NCM-S0	0.53	0.55	1.08
NCM-A1	0.39	0.93	1.33
NCM-A2	0.23	0.85	1.07

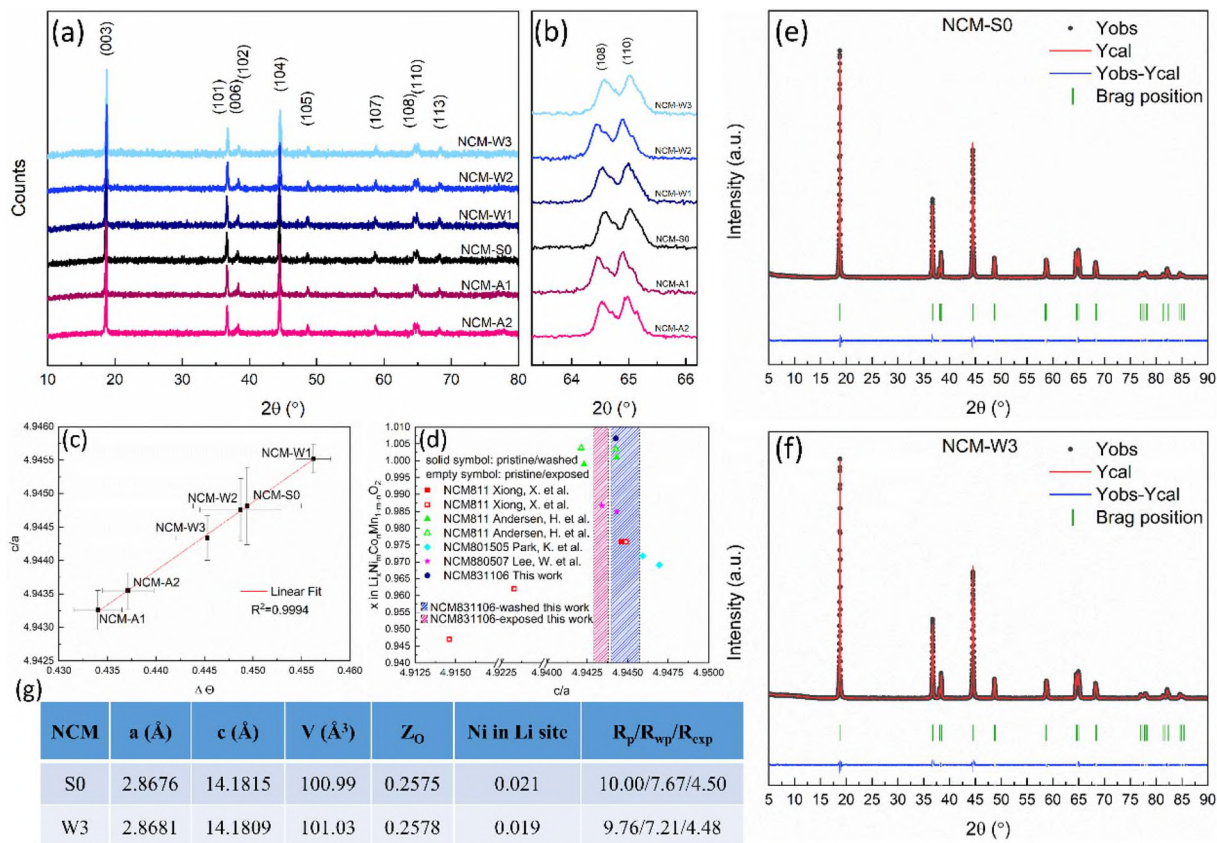


Fig. 1 (a) XRD patterns of different NCM83s.⁴ (b) Magnified image of (108) and (110) peaks for different NCM83s. (c) Relationship between the calculated c/a ratio from eqn (1) and $\Delta\theta$. (d) Relationship between the c/a ratio and Li stoichiometry x in $\text{Li}_x\text{Ni}_m\text{Co}_n\text{Mn}_{1-m-n}\text{O}_2$ obtained from the literature, in comparison with the c/a ratio range for NCM83s in this study (marked by the black line and shaded areas). High resolution XRD patterns (dark grey) and the corresponding Rietveld refinement analysis (red) of (e) NCM-S0 and (f) NCM-W3. (g) Rietveld refinement results of NCM-S0 and NCM-W3 showing the lattice parameters, a and c , unit cell volume, V , atomic coordinate of oxygen ions, Z_{O} , and occupation of Ni ions in Li sites.

lattice, c/a ratios can be calculated using eqn (1) based on the 2θ angles of (108) and (110) peaks,

$$\sin^2 \theta = A(h^2 + k^2 + hk) + Cl^2 \quad (1)$$

where $A = \lambda^2/3a^2$ and $C = \lambda^2/4c^2$. The plot of c/a ratios calculated from eqn (1) against $\Delta\theta$ for different NCM83s (Fig. 1c) is fitted well by using a linear function with an R^2 of 0.994. The c/a ratios of water-washed samples vary insignificantly from that of the pristine sample and reside mostly in the error bars of the pristine sample, indicating well-preserved bulk crystal structures after washing treatment. Meanwhile, the air-exposed samples show relatively smaller c/a ratios compared to the pristine sample, indicating a slight degradation of layered structures. However, the variation of c/a ratios for all samples is within a small range of 4.9433–4.9455. The c/a ratios and Li content x of pristine, water-washed and humid-air-exposed $\text{Li}_x\text{Ni}_m\text{Co}_n\text{Mn}_{1-m-n}\text{O}_2$ ($0.80 < m < 0.88$) reported in the literature are summarized and compared with those of NCM83s in Fig. 1d. Pristine $\text{Li}_x\text{Ni}_m\text{Co}_n\text{Mn}_{1-m-n}\text{O}_2$ with an x greater than 0.97 has c/a ratios within a range of 0.9443–0.9470, coinciding with that of pristine NCM83 (black line in Fig. 1d) in this study, indicating that pristine NCM83 has layered bulk crystal

structures. Although quite different washing conditions were adopted in the literature, c/a ratios vary insignificantly, and the Li content x changes by no more than 0.003 after water-washing as shown by ref. 30, 32, 34 and 38. c/a ratios of water-washed NCM83s (blue shaded area in Fig. 1d) have similar values to those reported in the literature, inferring that the bulk crystal structures of NCM83 remain layered after water-washing in this study. The reported crystal structures of air-exposed samples show large discrepancy possibly due to different storage conditions. NCM811 stored in a closed container for 9 weeks shows insignificant changes in c/a ratios and minor changes in x (empty green triangle),³⁸ while that stored in air for 30 days shows great reductions in the c/a ratio and x (empty black square).³² As NCM83s were stored in a closed container of humid air for no more than 18 hours in this study, their c/a ratios remain high (as shown by the pink shaded area in Fig. 1d), indicating the retention of layered bulk crystal structures.

Rietveld refinement was applied to NCM-S0 and NCM-W3 to precisely evaluate the bulk structural change of NCM83 after water treatment. The high-resolution XRD patterns were fitted by a rhombohedral crystal structure (space group $R\bar{3}m$) model where lithium, transition metals and oxygen ions occupy the 3b,

3a and 6c sites, respectively. The occupancies of Co, Mn and O ions were fixed based on cathode stoichiometry and elemental compositions measured by inductively coupled plasma-optical emission spectroscopy (ICP-OES) (Table S1†). Refinement of XRD peak shapes, unit cell lattice parameters, atomic coordinates of O ions and occupancies of Li and Ni ions in 3b and 3a sites was conducted. The fitted patterns match well with the observed ones (Fig. 1e and f). Detailed structural information obtained from Rietveld refinement is shown in Fig. 1g. The unit cell parameters for NCM-S0 are $a = 2.8676 \text{ \AA}$, $c = 14.1815 \text{ \AA}$ and $V = 100.99 \text{ \AA}^3$, and those for NCM-W3 are $a = 2.8681 \text{ \AA}$, $c = 14.1809 \text{ \AA}$ and $V = 101.03 \text{ \AA}^3$, indicating that the bulk crystal structure of NCM83 was not changed by water treatment. The c/a ratios are consistent with those calculated using eqn (1) and those reported in the literature (Fig. 1d). NCM-S0 and NCM-W3 also have similar oxygen atomic coordinates (Z_O) of 0.021 and 0.019, respectively, implying a similar inter-slab thickness. The occupation of Ni ions in Li sites is 0.021 and 0.019 for NCM-S0 and NCM-W3, respectively, suggesting invariant and low degree of cation disorder that is beneficial for Li diffusion in an NCM lattice.

The surface morphologies of pristine, water-washed and humid-air-exposed samples are shown in Fig. 2. The contours of primary particles become less distinct after water washing (Fig. 2b), probably due to the removal of surface Li residuals. After humid air-exposure, thin plate-like and film-like particles appear on the surface, which are probably the surface grown Li residuals.

The electrochemical performances of various NCM83s were characterized by using NCM/Li half cells at room temperature. The 1st-cycle voltage profiles (Fig. 3a) reveal that pristine NCM83 (NCM-S0) displays a reversible capacity of $191.1 \text{ mA h g}^{-1}$ at 0.1C with an initial coulombic efficiency of 87.4%. After water-washing treatment, NCM-W1, NCM-W2 and NCM-W3 show reversible capacities of 208.4, 210.6 and $212.8 \text{ mA h g}^{-1}$ at 0.1C and initial coulombic efficiencies of 93.6, 94.7 and 94.9%, respectively, which gradually increase with increasing water/NCM ratio. Meanwhile, humid-air exposed samples NCM-

A1 and NCM-A2 also show slightly increased reversible capacities of 196.8 and 197 mA h g^{-1} at 0.1C and slightly increased initial coulombic efficiencies of 90.1 and 90.5%, respectively.

The 1st- and 2nd-cycle dQ/dV vs. V curves (Fig. 3b and c) display the characteristic redox peaks of NRLOs, indicating phase transformations from hexagonal phase 1 (H1) into monoclinic phase (M), and then into hexagonal phase 2 (H2) and hexagonal phase 3 (H3) during delithiation and *vice versa* during lithiation.³⁹ It is clearly observed that the increase in reversible capacity at 0.1C after water-washing and humid air-exposure stems from the improved reversibility of H1 phase transformations at the end of discharge (3.40–3.75 V vs. Li/Li⁺), which means that more Li can be intercalated back into NCM lattices. The larger capacity loss for NRLOs at the end of discharge is attributed to kinetic hindrances to Li ion diffusion in the NCM lattice.^{23,24,27} It has been shown that Li migration in layered transition metal oxides is predominantly governed by the tetrahedral site hop mechanism (TSH) where the migrating Li ion located in an octahedral site passes through a face-sharing tetrahedral site before reaching an octahedral vacant site²¹ (as shown in the schematic illustration in Fig. 3d). The activation barrier for Li migration is governed by both electrostatic interactions between the migrating Li and neighboring Li ions or cations and the size of the tetrahedral site.⁸ For TSH pathways, the Li migration barrier declines as the concentration of Li vacancies increases,²¹ which means that the high occupancy of Li sites at a low state of charge (SOC) escalates the activation barrier for Li migration and hence impedes Li intercalation back into NCM lattices. During water-washing and humid air-exposure treatments, Li-H₂O interactions induce chemical delithiation of NCM83 and create more Li vacancies in the surface region of the NCM lattice. The formation of Li vacancies and rearrangement of local structures may lower the energy barrier to lithium diffusion and create fast Li transport channels, which facilitates Li migration in the NCM lattice at low SOC and increases reversible capacities. Since the reaction between NCM83 and water is milder during humid-air exposure than during water washing, the exposed samples show less

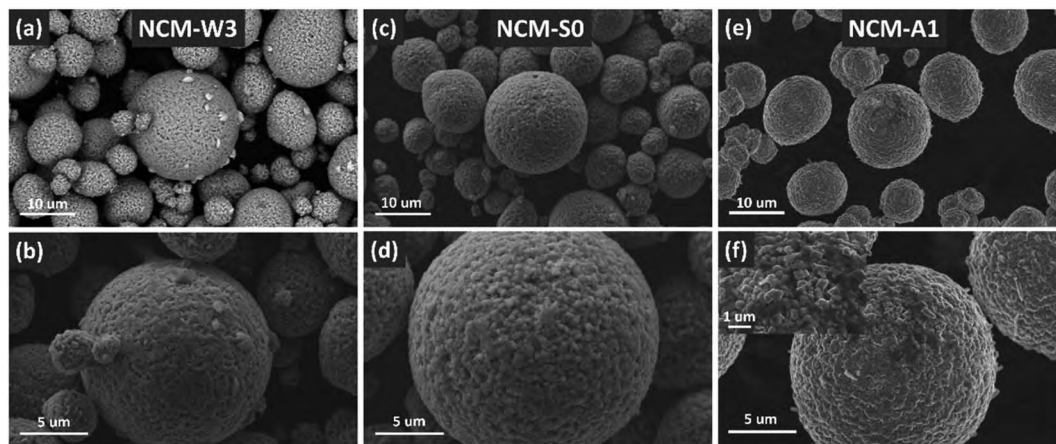


Fig. 2 SEM images of (a and b) water-washed NCM83, (c and d) pristine NCM83 and (e and f) humid air-exposed NCM83 at different magnifications.

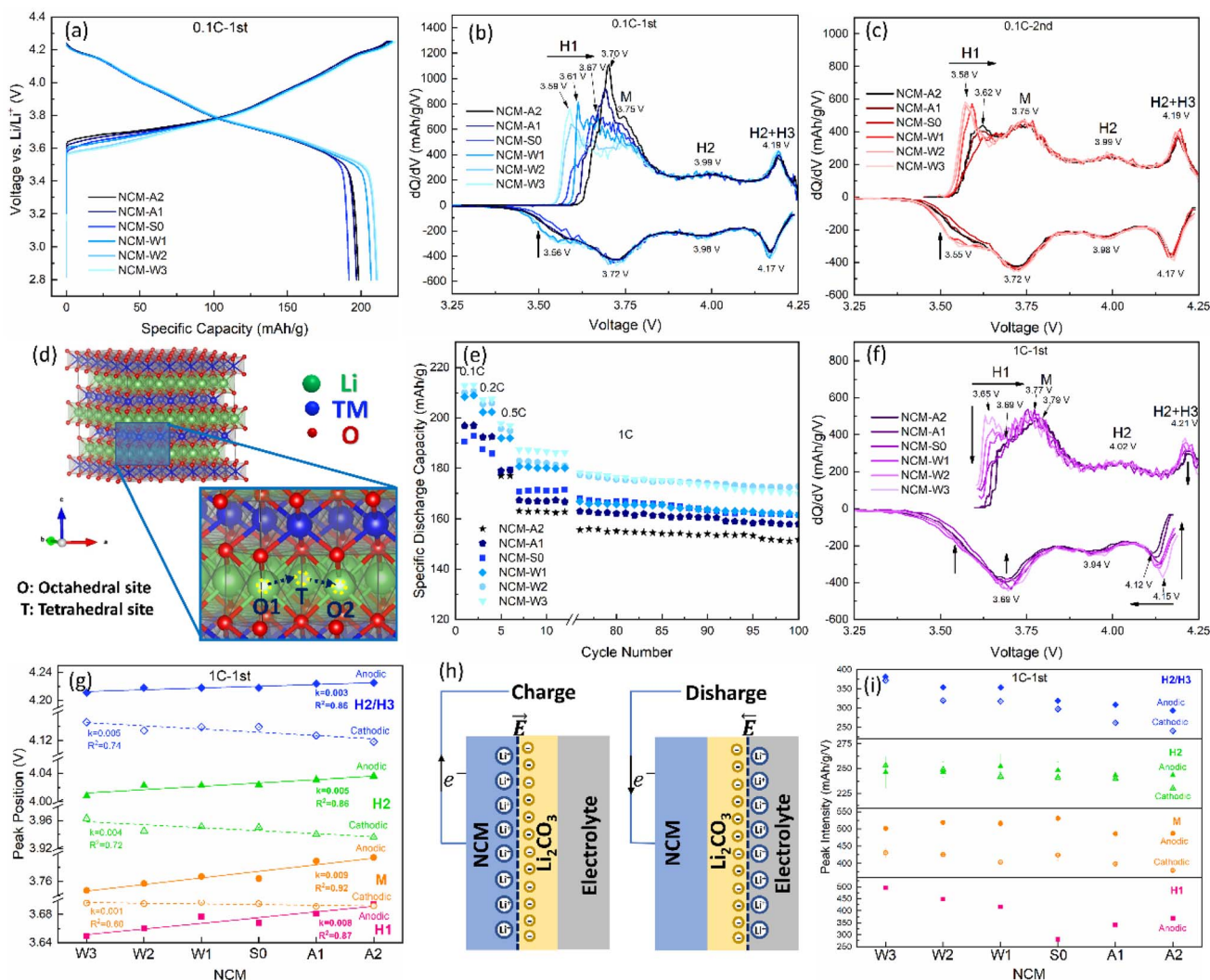


Fig. 3 (a) 1st-cycle voltage profiles for different NCM83s. (b) 1st-cycle dQ/dV vs. V curves for different NCM83s. (c) 2nd-cycle dQ/dV vs. V curves for different NCM83s. (d) Schematic illustration showing the mechanism of Li diffusion in layered NCM83s. (e) Rate and cycling performance of different NCM83s. (f) 1st-cycle dQ/dV vs. V curves at 1C for different NCM83s. (g) Summary of the peak positions of electrochemical redox peaks for different NCM83s shown in (f). (h) Schematic illustration showing the inhibition of Li transfer by Li_2CO_3 and formation of a space charge layer and interfacial electric field during charge/discharge. (i) Summary of the peak intensities of electrochemical redox peaks for different NCM83s shown in (f).

enhanced electrochemical reaction kinetics and reversible capacities in the low-SOC region as compared with the washed samples. As the concentration of Li vacancies increases in medium- and high-SOC regions, Li diffusions in all NCM83s are ameliorated. The kinetics of electrochemical reactions in all NCM83s are therefore enhanced with high consistency as shown in Fig. 3b and c. Although Ni ions can migrate into Li layers during chemical delithiation of NRLOs, it has been shown that the strong interactions between Ni ions in the Li layer and O ions can drive the diffusion of Li ions in the nearest sites of Ni ions.⁴⁰

As charge/discharge rates increase, the reversible capacity of NCM83 has strong correlation with the concentration of surface Li_2CO_3 . At 1C, the reversible capacity decreases with increasing concentration of Li_2CO_3 (Fig. 3e), indicating that resistive

Li_2CO_3 leads to a large charge transfer resistance across the cathode/electrolyte interface, degrading the rate performance of NCM83. Fig. 3f reveals the 1st-cycle dQ/dV vs. V curves for different NCM83s. The positions of all the characteristic peaks are summarized in Fig. 3g. It shows that with increasing Li_2CO_3 concentration, the anodic peaks (solid symbols in Fig. 3g) experience shifts to higher voltages and the degree of shifting decreases as the SOC increases. In contrast, the cathodic peaks (empty symbols in Fig. 3g) display shifts to lower voltages and the degree of shifting decreases as SOC decreases. The more significant polarization effect at the beginning of charge and discharge processes is related to the large Li migration barrier caused by Li_2CO_3 . While Li_2CO_3 electrochemically decomposes at an onset voltage of ~ 3.9 V, a portion of Li_2CO_3 is expected to remain at the cutoff voltage of 4.25 V vs. Li/Li^+ used in this

study.⁴¹⁻⁴³ As charge begins, due to low Li-ion conductivity of Li_2CO_3 , Li ion transfer across the NCM83/ Li_2CO_3 interface is impeded and Li ions are accumulated at the NCM83 side, causing accumulation of electrons at the Li_2CO_3 side and formation of a space charge layer (SCL) (Fig. 3h). The gradually built interfacial electric field then facilitates Li ion transportation across the NCM83/ Li_2CO_3 interface and mitigates the polarization effect as charge proceeds. During the discharge process, Li ion transfer is initially inhibited at the electrolyte/ Li_2CO_3 interface, leading to Li ion accumulation at the electrolyte side and electron accumulation at the Li_2CO_3 side

(Fig. 3h). The interfacial electric field then promotes Li ion transfer across the electrolyte/ Li_2CO_3 interface and reduces polarization as discharge continues. Moreover, Li_2CO_3 has great impact on the activities of electrochemical reactions. Fig. 3i shows that the intensities of the characteristic peaks in 1st-cycle dQ/dV vs. V curves at 1C reduce with increasing Li_2CO_3 concentration, and the degree of reduction is more significant in low- and high-SOC regions. The NRLO cathode suffers from kinetic hindrance at low- and high-SOC due to the increase in Li concentration in the NRLO lattice and decrease of interlayer spacing, respectively.¹¹ Resistive Li_2CO_3 on the NCM surface

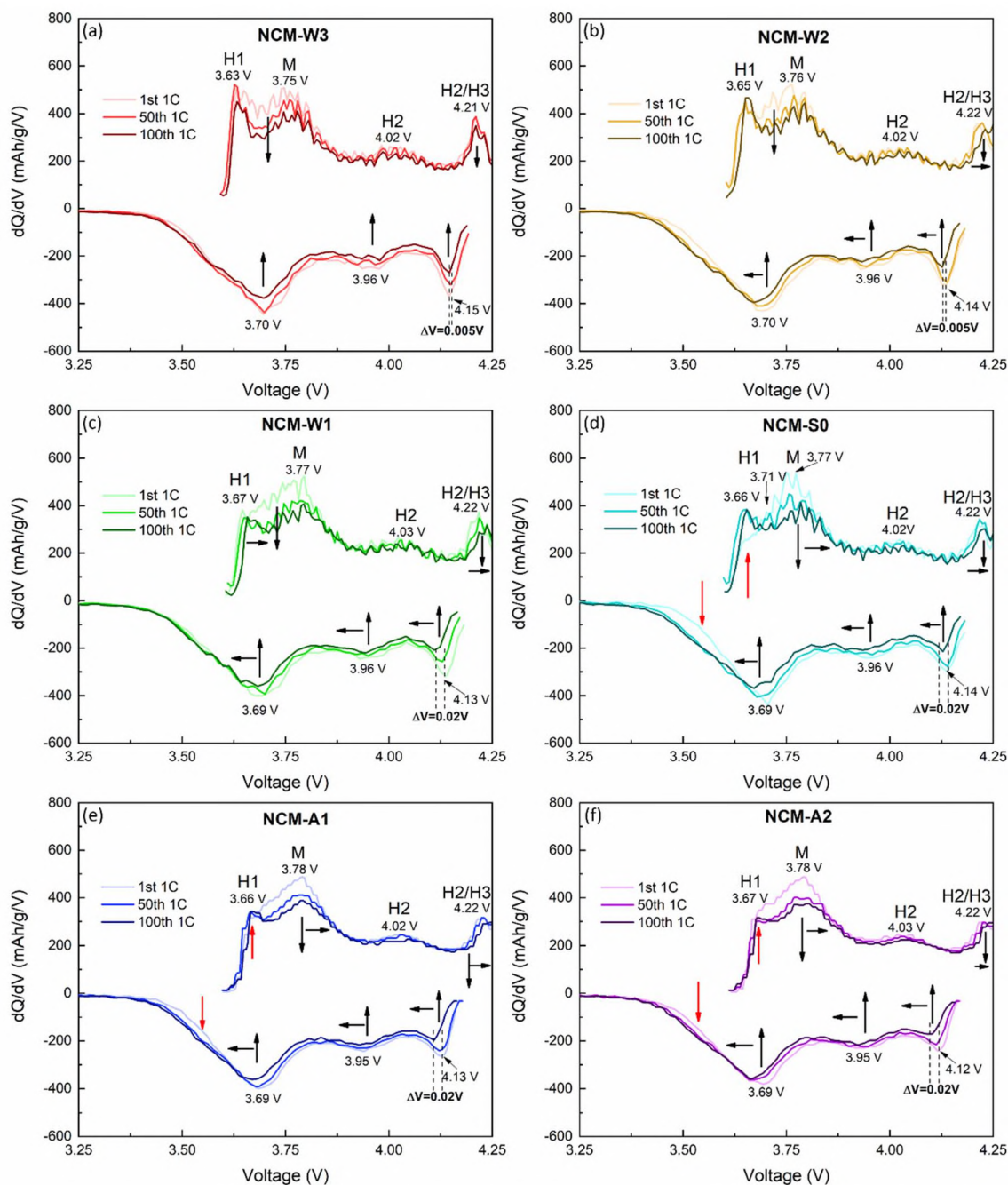


Fig. 4 dQ/dV vs. V curves for (a) NCM-W3, (b) NCM-W2, (c) NCM-W1, (d) NCM-S0, (e) NCM-A1, and (f) NCM-A2 at different cycles.

enlarges the kinetic hindrance to Li diffusion and hence inhibits the electrochemical reactions in these regions.

The cycling performance at 1C (Fig. 3e) shows that the capacity retention rates over 100 cycles for NCM-W3, W2, W1, S0, A1 and A2 are 89.4%, 92.7%, 88.2%, 92.4%, 93.6% and 91.9%, respectively. Fig. 4 further reveals that dQ/dV vs. V curves shift more significantly over 100 cycles as the concentration of Li_2CO_3 increases, indicating that surface Li_2CO_3 increases the overpotential over cycling and degrades the cycling stability of NCM83. This can be attributed to the exaggerated side reactions between Li_2CO_3 and electrolyte over cycling, as Li_2CO_3 decomposes at high voltages to create singlet oxygen, facilitating further electrolyte decomposition and accumulation of resistive compounds such as LiF , Li_2O , P_2O_5 and Li_xPOF_y at cathode/electrolyte interfaces.^{12,43,44} However, it should be noted that the H1 phase transformation of NCM-W2, S0, A1 and A2 is enhanced over cycling, which leads to increased reversible capacities over cycling and high capacity retention rates. This is ascribed to the creation of more Li vacancies in the NCM83 lattice due to the irreversible intercalation of Li ions. As Li vacancies build up and rearrange over cycling, Li diffusion at

low-SOC is enhanced and the reversibility of H1 phase transformation is improved.

Li transport across the cathode/electrolyte interface was studied by electrochemical impedance spectroscopy (EIS) in detail. EIS measurements were conducted at ~ 3.6 V vs. Li/Li^+ during different charge cycles. NCM-S0 and NCM-W3 were selected as representative samples to investigate the effect of surface modification of NCM83 on charge transport across the cathode/electrolyte interface over cycling. The open-circuit voltage (OCV) of different samples was controlled at similar values to minimize the influence of SOC on EIS spectra. The EIS spectra of NCM-S0 and NCM-W3 at 3.6 V during different charge cycles (Fig. 5a-d) reveal three semicircles followed by a linear tail from high to low frequencies. The electrical equivalent circuit used to fit the EIS spectra is shown in Fig. 5b. The semicircle at high frequency (HF) (>1 kHz) generally describes Li transport through the cathode/electrolyte interphase (CEI) layer,⁴⁵ which is modelled by resistance (R_{HF}) connected in parallel with a constant phase element (CPE and CPE_{HF}). CEI layers of NCM-S0 and NCM-W3 display capacitances in the μF range (Fig. 5a), consistent with that shown by the

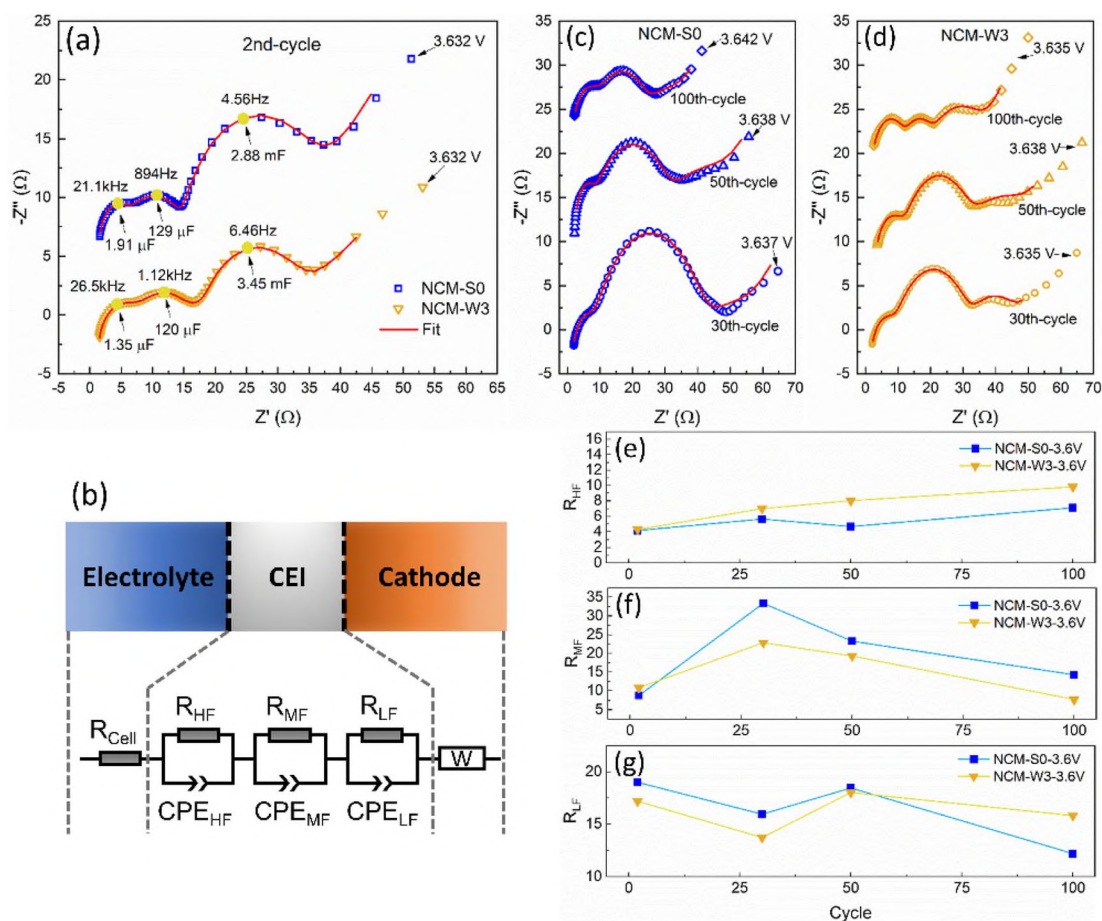


Fig. 5 (a) EIS of NCM-S0 and NCM-W3 measured at 3.632 V vs. Li/Li^+ during the 2nd charge cycle and fitted by using an electrical equivalent circuit. (b) Schematic diagram showing the equivalent circuit that describes the ion transport in different regions at the cathode side of Li-ion battery cells. EIS of (c) NCM-S0 and (d) NCM-W3 measured at ~ 3.6 V during different charge cycles and fitted by using an electrical equivalent circuit. Variations of (e) R_{HF} , (f) R_{MF} and (g) R_{LF} of NCM-S0 and NCM-W3 over cycling.

$\text{Li}_x\text{Co}_{0.2}\text{Ni}_{0.8}\text{O}_2$ cathode.⁴⁶ Semicircles within the frequency range of 10 mHz to 1 kHz correspond to the charge transfer processes from the electrolyte to CEI and from the CEI to cathode active materials.^{45,47} It is difficult to discretize explicitly different transport and charge transfer processes. The charge transfer process across the CEI/active material interface for the $\text{Li}_x\text{Co}_{0.2}\text{Ni}_{0.8}\text{O}_2$ cathode displays capacitances in the order of mF.⁴⁶ Therefore, the low-frequency (LF) semicircle modelled by $R_{\text{LF}}/\text{CPE}_{\text{LF}}$ is assigned to charge transfer from the CEI to active cathode materials, and the middle-frequency (MF) semicircle modelled by $R_{\text{MF}}/\text{CPE}_{\text{MF}}$ is believed to represent charge transfer from the electrolyte to the CEI. R_{cell} at higher frequencies ($\sim 10^4$ Hz) represents the total resistance to Li transport through the electrolyte and separator. A Warburg element (W) is used in the lowest-frequency region to describe the solid-state diffusion of

Li ions within cathode particles. Charge transfer across the anode/electrolyte interface may also contribute to the semicircle in the LF range.⁴⁸ As the anode was kept the same for all Li-ion battery cells, the variation of EIS spectra between different NCM83 samples is believed to reflect the change of Li diffusion and charge transfer processes at the cathode side due to cathode surface modification. The fitting results of all EIS spectra are shown in Fig. 5e–g. It is shown that R_{LF} of NCM-W3 is lower than that of NCM-S0 at different cycles, possibly due to the removal of resistive surface Li residuals and modification of surface crystal structures (as discussed below) of NCM83 by controlled water treatment. The relatively larger R_{LF} of NCM-W3 at the 100th cycle is due to the lower SOC of NCM-W3.⁴⁹ Moreover, NCM-S0 displays much higher R_{MF} compared to NCM-W3 as cycling proceeds, indicating that the high charge transfer

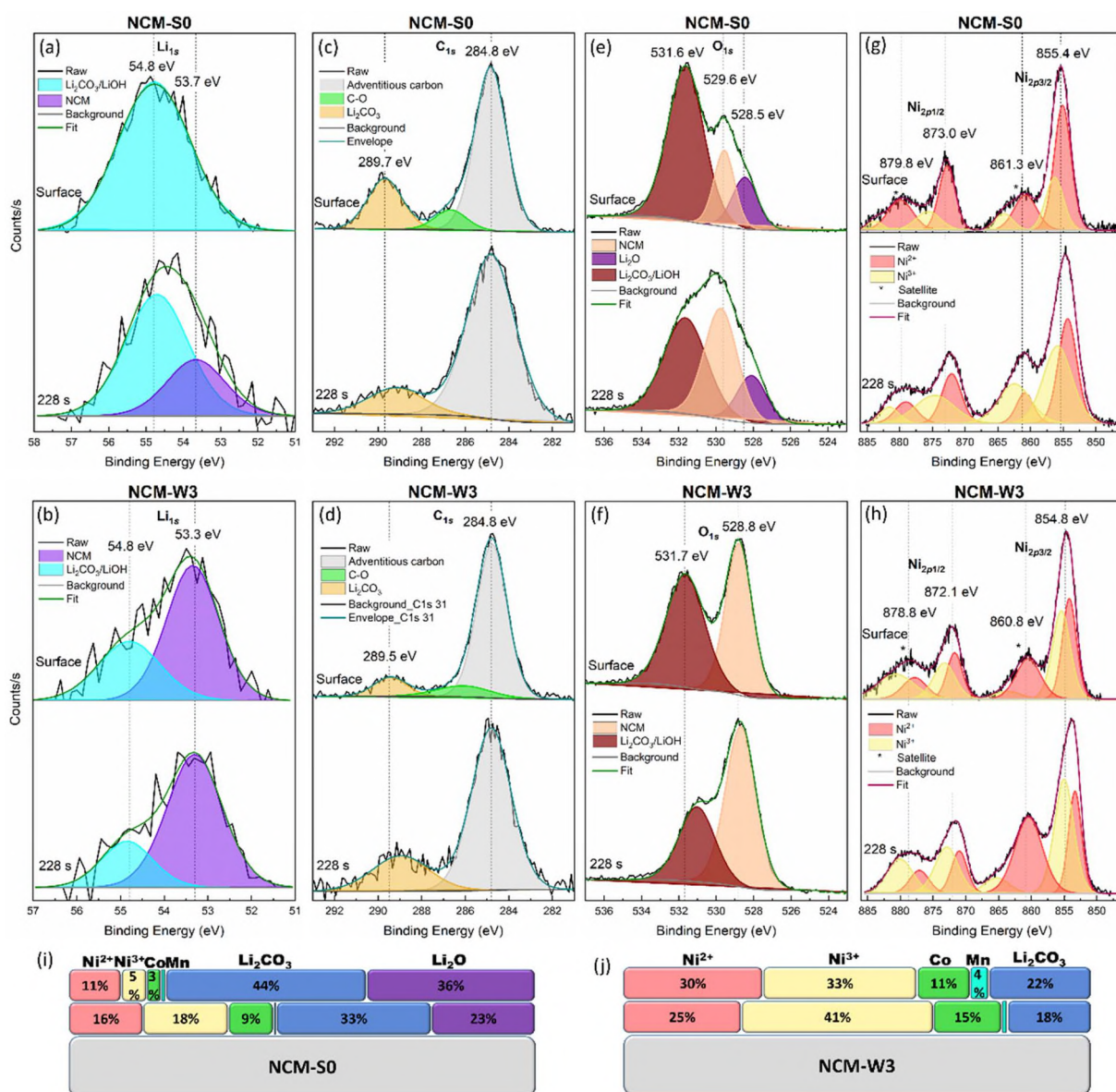


Fig. 6 XPS Li_{1s} spectra of (a) NCM-S0 and (b) NCM-W3. C_{1s} spectra of (c) NCM-S0 and (d) NCM-W3. O_{1s} spectra of (e) NCM-S0 and (f) NCM-W3. Ni_{2p} spectra of (g) NCM-S0 and (h) NCM-W3. Percentages of chemical components at the surface of (i) NCM-S0 and (j) NCM-W3.

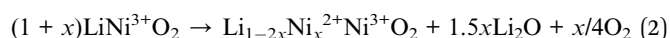
resistance across the electrolyte/CEI interface is mainly responsible for the increased polarization over cycling for those NCM83 samples with high surface Li_2CO_3 contents. As the electrochemical decomposition of Li_2CO_3 generates singlet oxygen and triggers electrolyte decomposition,^{11,12,43,44} resistive species may form on the surface of the initially formed CEI layer, impeding charge transfer across the electrolyte/CEI interface. Over cycling, R_{MF} decreases significantly, likely due to the reconstruction of the resistive layer to form favourable Li ion transport pathways. R_{HF} of NCM-S0 and NCM-W3 vary insignificantly and remain at a low value $<10 \Omega$ over cycling, which may have insignificant effects on charge transport and cycling performance of different NCM83s.

To investigate the difference in surface Li residual species and surface crystal structures between different NCM83s, NCM-S0 and NCM-W3 were characterized by XPS depth profiling for comparison. The Li_{1s} spectrum of NCM-S0 (Fig. 6a) shows a single peak at 54.8 eV, indicating the presence of abundant $\text{LiOH}/\text{Li}_2\text{CO}_3$ (ref. 11, 31, 43 and 44) on the NCM-S0 surface. After etching, the concentration of $\text{LiOH}/\text{Li}_2\text{CO}_3$ decreases significantly (Table S1†) and the signal associated with the NCM lattice appears at 53.7 eV.^{12,45} In contrast, the Li_{1s} spectrum of NCM-W3 (Fig. 6b) reveals two distinctive peaks at 53.3 and 54.8 eV, corresponding to Li in the NCM lattice and surface $\text{LiOH}/\text{Li}_2\text{CO}_3$, respectively. After etching, the atomic ratio between two components varies insignificantly (Table S2†), indicating the low content of Li residuals on the NCM-W3 surface. The C_{1s} spectra of NCM-S0 (Fig. 6c) and NCM-W3 (Fig. 6d) show two main peaks at 284.8 and ~ 289.6 eV, corresponding to adventitious carbon and Li_2CO_3 ,^{30,55} respectively. The peak at ~ 286 eV is assigned to C–O bonds.⁵⁶ NCM-S0 has a higher content of Li_2CO_3 than NCM-W3 (Tables S1 and S2†) confirming the successful removal of Li_2CO_3 by water-treatment. After etching, the concentration of Li_2CO_3 on the NCM-S0 surface declines while that on the NCM-W3 surface is retained (Tables S1 and S2†).

The O_{1s} spectra (Fig. 6e and f) reveal more details about Li residual species and crystal structures at surfaces of different NCM83s. The peak at 531.7 eV corresponding to $\text{LiOH}/\text{Li}_2\text{CO}_3$ (ref. 32, 42, 46, 47, 50 and 51) again corroborates the existence of more $\text{LiOH}/\text{Li}_2\text{CO}_3$ on the surface of NCM-S0 than on that of NCM-W3. After etching, the $\text{LiOH}/\text{Li}_2\text{CO}_3$ peak of NCM-S0 drops considerably and that of NCM-W3 drops and shifts to a lower binding energy of ~ 531 eV attributable to defective oxygen at the surface of Ni-based metal oxides.⁵³ This indicates that etching removes the small amounts of Li residuals on the NCM-W3 surface, causing more of the NCM lattice to be exposed. Furthermore, in the O_{1s} spectrum of NCM-S0, a distinctive peak appears at 528.5 eV which is assigned to Li_2O .^{48,49,59,60} The concentration of Li_2O decreases after etching, indicating its presence at the surface. Fig. 6i shows that Li_2O is a major component of Li residuals on the NCM-S0 surface. After water-washing, they are completely removed as shown by the O_{1s} spectrum of NCM-W3.

The peaks at 529.6 and 528.8 eV in the O_{1s} spectrum of NCM-S0 (Fig. 6e) and NCM-W3 (Fig. 6f), respectively, are assigned to O in the NCM lattice. The different peak positions of lattice oxygen

indicate that the surface lattice structures of NCM-S0 and NCM-W3 are quite different. The O_{1s} peak at 529.5 eV is commonly found in NiO and $\text{Li}_{0.3}\text{Ni}_{0.7}\text{O}$ with rock-salt crystal structures,^{30,54} inferring that the surface of NCM-S0 is converted to $\text{Li}_x\text{Ni}_{1-x}\text{O}$ -type rock-salt phases. This is probably caused by oxygen evolution during high-temperature synthesis, especially when the oxygen chemical potential in the atmosphere is low.⁶¹ As the oxygen vacancy formation energy and oxygen migration barrier are lower on the surface than in the bulk of NRLOs, oxygen evolution is more favorable at the NCM83 surface. The oxidation and evolution of lattice oxygen leave electrons to neighbouring Ni atoms and provide migration pathways for Ni atoms.⁶² Ni^{3+} ions are then reduced to Ni^{2+} ions and migrate to Li layers.⁶² As the Li stoichiometry at the NCM-S0 surface decreases to less than ~ 0.62 ,^{36,37} layered phases are converted into $\text{Li}_x\text{Ni}_{1-x}\text{O}$ -type rock-salt phases. This process is accompanied by Li_2O extraction following eqn (2)³⁷



which explains the formation of Li_2O on the NCM-S0 surface. Besides, Li_2O may be also generated from the decomposition of residual LiOH ³⁴ which was used as a Li precursor. Some Li_2O may react with O_2 to form Li_2O_2 and evaporate during the synthesis,⁶³ accounted for as the lithium loss.⁶⁴ The residual Li_2O and LiOH react with CO_2 during and after the synthesis to form Li_2CO_3 on the NCM-S0 surface.

On the other hand, the lattice oxygen peak of NCM-W3 at 528.8 eV is only found in LiNiO_2 (ref. 12 and 45) and is close to that of NRLOs (529 eV) generally seen in the literature,^{14,30,38,57,58} indicating that the surface of NCM-W3 has a layered structure. It has been proposed that transition metal carbonate (-hydroxide) hydrates¹⁶ or $\text{MO}(\text{OH})$ -like (M stands for transition metals)³¹ compounds form on the surface of NRLOs after exposure to water. If those compounds were generated during water treatment of NCM-W3, they should have decomposed to transition metal oxides at 450 °C during the sequential thermal treatments.^{31,65,66} However, the lattice oxygen peaks of spinel or rock-salt transition metal oxide compounds⁶⁷⁻⁷⁰ do not exist at such a low binding energy of 528.8 eV. This shows that the mild washing conditions used in this study prevent the formation of a resistive NiO-like layer on the NCM83 surface. Instead, $\text{Li-H}_2\text{O}$ interactions probably extract the Li ions from the outermost surface and cause Li ions to migrate from the bulk to the surface,⁷¹ replenishing the Li content at the surface. During the sequential heat treatment in an O-rich environment, Li ions and vacancies in the surface region are redistributed, resulting in a surface layer with a Li content exceeding 0.62 and hence, a layered structure with Li vacancies.

The 2p spectra of Ni show multiplet splitting and shake-up peaks due to the final-state effect and charge transfer between Ni ions and neighbouring oxygen ions.^{54,72} The main $\text{Ni}_{2p3/2}$ peak of NCM83 can be deconvoluted into two peaks corresponding to Ni^{2+} and Ni^{3+} ions, respectively.^{52,57} The binding energy difference between $\text{Ni}_{2p3/2}$ and $\text{Ni}_{2p1/2}$ peaks for Ni^{2+} ions in NCM83 is 17.66 eV, coinciding with that for Ni^{2+} ions in NiMoO_4 .⁷³ The concentration of Ni^{2+} is significantly higher than

that of Ni^{3+} at the surface of NCM-S0 (Fig. 6g and i), confirming that the surface of NCM-S0 has a $\text{Li}_x\text{Ni}_{1-x}\text{O}$ -type rock salt structure with predominant Ni^{2+} ions. On the other hand, the concentration of Ni^{3+} ions is similar to that of Ni^{2+} ions on the NCM-W3 surface (Fig. 6h and j), indicating the presence of more layered phases at the surface of NCM-W3. After etching, the Ni^{3+} peaks of NCM-S0 and NCM-W3 grow as more Ni^{3+} ions are present in the bulk of NCM83. The shift of Ni_{2p} peaks accompanied with etching originates from the reduction of Ni ions by Ar^+ beams.⁷⁴

The Mn_{2p} spectra of NCM-S0 and NCM-W3 reveal that the Ni LMM Auger peak centered at 643.6 eV and spanning across a wide binding energy range of 631.6 to 654.1 eV overlaps with the $\text{Mn}_{2p_{3/2}}$ peak located at ~ 642 eV, leading to a broad peak (Fig. S1a and b[†]). Therefore, it is not feasible to deconvolute the Mn_{2p} spectra to obtain detailed information on the chemical state of Mn ions. The Co_{2p} spectra of NCM-S0 and NCM-W3 display a significant multiplet splitting effect (Fig. S1c and d[†]). The $\text{Co}_{2p_{3/2}}$ peak centered at ~ 780 eV is assigned to Co^{3+} ions.^{72,75} As the etching time increases, the peaks become

broadened and the final state effect becomes more significant, leading to more prominent satellite peaks. The Co/Mn concentrations derived from the peak areas of $\text{Co}_{2p_{3/2}}/\text{Mn}_{2p_{1/2}}$ peaks are shown in Fig. 6i and j. The atomic ratios among Ni/Co/Mn at NCM-S0 and NCM-W3 surfaces are 81/16/3 and 80/15/5, respectively. These values are consistent with those after etching (Tables S3 and S4[†]), which match well with the theoretical stoichiometry of $\text{LiNi}_{0.83}\text{Co}_{0.11}\text{Mn}_{0.06}\text{O}_2$.

NCM-S0 and W3 were also characterized by HRTEM to obtain a clearer view of surface species and crystal structures. A 6 nm-thick amorphous layer is discovered on the surface of NCM-S0 (Fig. 7a), which is possibly the surface Li_2CO_3 species. Underneath the amorphous layer, lattices of Li_2O are found, showing the (012) crystal planes, which matches with the XPS results. In the inner region, (003) crystal planes of the NCM lattice are observed with an interlayer spacing of 4.72 Å, which coincides well with that (4.74 Å) measured by XRD. Fig. 7b shows that the surface of NCM-S0 is composed of $\text{Li}_x\text{Ni}_{1-x}\text{O}$ -type rock-salt phases, which again corroborates the XPS results. The distribution of Ni, Co, Mn and O at the NCM-S0

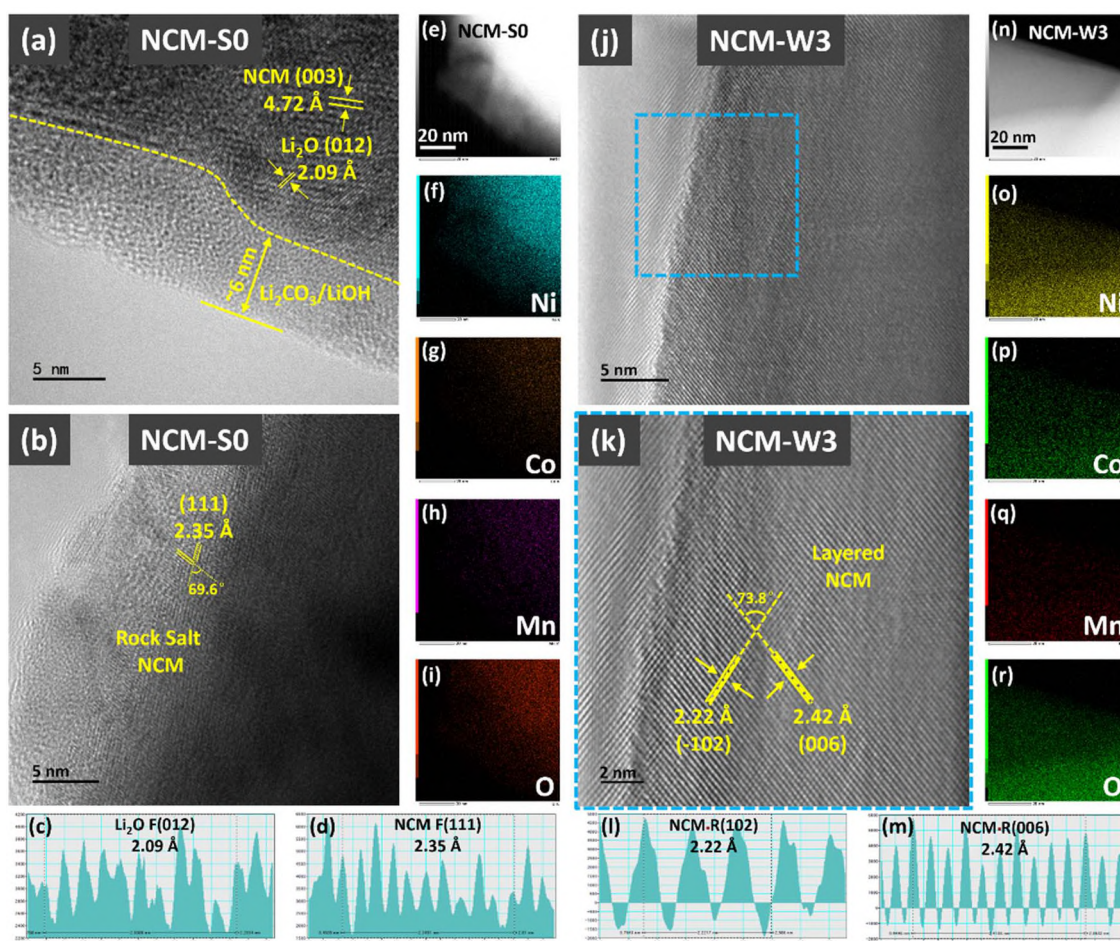


Fig. 7 HRTEM of (a) NCM-S0 covered by Li residuals and (b) NCM-S0 with $\text{Li}_x\text{Ni}_{1-x}\text{O}$ type rock salt structures at the surface. The line profile across (c) (012) crystal planes of Li_2O at the surface of NCM-S0 and (d) (111) crystal planes of NCM-S0 with $\text{Li}_x\text{Ni}_{1-x}\text{O}$ -type rock salt structures. (e–i) STEM dark field image and EDS mapping of NCM-S0. HRTEM of (j) NCM-W3 with a clean surface and (k) a close-up image of the surface crystal structure in the blue-square region in (j). Line profile across (l) (102) crystal planes of NCM-W3 with layered structures, (m) (006) crystal planes of NCM-W3 with layered structures, (n–r) STEM dark-field image and EDS mappings of NCM-W3.

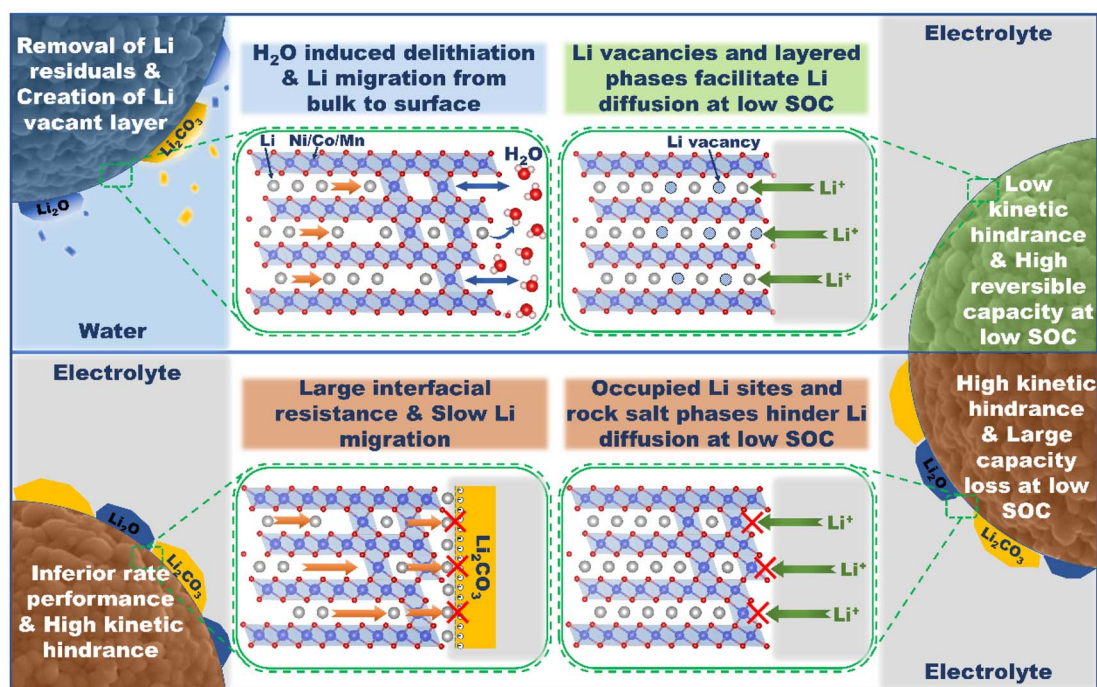


Fig. 8 Schematic diagram showing the evolution of surface Li residuals and crystal structures of NCM83 after water-washing, and the effects of Li residuals/Li vacancies on electrochemical performance of NCM83s.

surface is shown by EDS mappings (Fig. 7e–i). In contrast, Li residual species are not observed on the surface of NCM-W3 after water-treatment (Fig. 7j). A closer view of the surface lattice structure (Fig. 7k) indicates that the spacing between (003) crystal planes expands to 4.84 Å (as compared with 4.72 Å measured by XRD) and the spacing between (102) crystal planes contracts to 2.22 Å (2.34 Å measured by XRD). (003) crystal planes are perpendicular to the lattice parameter c , and the expansion of the inter-planar spacing indicates an increase in c . The spacing between (102) crystal planes is affected by both lattice parameters c and a , and the decreased inter-planar spacing means contraction in a . It is well known that c increases and a decreases as the Li content in layered NRLOs decreases from 1 to 0.6 during electrochemical delithiation, and the layered structure is maintained.⁷⁶ Therefore, it confirms that layered phases with Li vacancies are formed at the surface of NCM-W3. The distribution of Ni, Co, Mn and O at the NCM-W3 surface is shown by EDS mappings (Fig. 7n–r).

The evolution of surface Li residuals and crystal structures of NCM83s after water-treatment and the effects of Li residuals/Li vacancies on electrochemical performance of NCM83s are summarized in a schematic illustration (Fig. 8). During water-washing treatment, surface Li residuals (Li_2O and Li_2CO_3) dissolve in water. The exposed NCM83 then reacts with water, leading to minor chemical delithiation at the outermost surface of NCM83. $\text{Li}-\text{H}_2\text{O}$ interactions further induce the migration of Li ions from the bulk to the surface, replenishing the Li content in the surface region. By conducting heat treatment in an oxygen-rich environment afterwards, the surface structure reconstructed to layered phases with Li vacancies. During

electrochemical de/lithiation, the layered surface structures with Li vacancies greatly improve the Li diffusion in the NCM83 lattice at low SOC, leading to enhanced reversible capacities at the end of discharge. In contrast, a surface $\text{Li}_x\text{Ni}_{1-x}\text{O}$ -type rock salt structure without Li vacancies significantly impedes Li diffusion in NCM83 at low SOC, causing large capacity loss at the end of discharge. Meanwhile, surface Li_2CO_3 with low ionic conductivity causes large impedance against Li migration at the NCM83/ Li_2CO_3 interface, which leads to large polarization and degraded rate performance. Due to kinetic-hindrance effects at low and high SOC, the slow Li migration in Li_2CO_3 also inhibits the electrochemical reactions in these regions, resulting in reduced reversible capacities.

This water treatment method uses an environmentally friendly solvent to modify the surface chemical environment and crystal structures of a Ni-rich layered oxide (NRLO) cathode. Detrimental surface Li residual species are removed within several minutes under appropriate control of the water to NRLO ratio. After thermal treatment, favorable surface layered structures with Li vacancies are created, facilitating fast Li diffusion within the NRLO lattice at a low state of charge. This strategy allows significant improvement in battery performance within a short amount of time at a low cost, showing high potential for application in battery industries.

3 Conclusions

In this study, $\text{LiNi}_{0.83}\text{Co}_{0.11}\text{Mn}_{0.06}\text{O}_2$ (NCM83) was subjected to controlled water treatment which created Li-vacant layered structures and removed Li residuals at the surface of NCM83.

The electrochemical characterization revealed that surface Li vacancies played important roles in boosting Li migration in the NCM83 lattice, which improved the reversibility of the H1 phase transformation of NCM83 and hence, the 1st cycle reversible capacity. Additionally, the removal of Li residuals enhanced Li ion transport across cathode/electrolyte interfaces and suppressed side reactions induced by Li_2CO_3 decomposition, improving the rate performance and cycling stability of NCM83. Therefore, this facile strategy enhanced Li transport kinetics in NCM83 through modification of its surface structures and chemical environment, leading to significantly improved electrochemical performances.

4 Experimental

4.1 Cathode material preparation

For water-washing treatment, $\text{LiNi}_{0.83}\text{Co}_{0.11}\text{Mn}_{0.06}\text{O}_2$ (NCM83) cathode materials (NCM-S0) were mixed with de-ionised water at 1 : 0.5, 1 : 1 and 1 : 1.5 NCM83 to water ratios. The mixture was stirred in an ambient atmosphere at room temperature for a few minutes. NCM83 was later filtered and dried at 110 °C to remove the water. Subsequently, the washed NCM83s were annealed in an oxygen rich environment at 450 °C to obtain NCM-W1, NCM-W2 and NCM-W3. For humid air exposure treatment, NCM-S0 was placed in a closed container. The humidity inside the container was controlled at 77% by using a saturated NaCl solution, and the environment temperature was controlled at 30 °C. NCM-S0 was stored for 1.5 and 18 hours and then dried in a vacuum oven at 60 °C for 6 hours followed by drying at 120 °C for 12 hours to obtain NCM-A1 and NCM-A2.

4.2 Materials characterization

4.2.1 Measurement of surface Li residuals. HCl titration was used to measure the concentrations of Li_2CO_3 and LiOH on the NCM83 surface. The titrant solution was prepared by stirring NCM83 powders in de-ionized water for 30 min followed by filtration. 0.05 mol per L HCl solution was used to titrate the solution with phenolphthalein and methyl red indicators. The concentrations of Li_2CO_3 and LiOH were then derived from the titrate volume of HCl solution.

4.2.2 Physical and chemical characterization. XRD was conducted using an XD2 (Beijing Purkinje) with a Cu radiator (1.54056 Å) at a voltage of 36 kV and a current of 20 mA. The scanning rate was 8° per minute. For Rietveld refinement analysis, XRD patterns were collected using Bruker D8 X-Ray Diffractometer. The scan was conducted between 5 and 90 degrees at a step of 0.01 degree. The scanning speed is 0.05 degree per min.

SEM was conducted using a Phenom ProX (Phenom-Scientific) electron microscope with an acceleration voltage of 10 kV. The images were obtained under secondary electron detection mode.

TEM was conducted using a JEOL (JEM-F200) electron microscope with an acceleration voltage of 200 kV. The TEM images were obtained under the HR-TEM mode, and the images for EDS were captured under the STEM mode.

X-ray photoelectron spectroscopy (XPS) was performed by using a PHI 5000 VersaProbe III with a monochromatic Al K α X-ray source with a beam size of 200 μm . Charge compensation was achieved by dual beam charge neutralization and the binding energy was corrected by setting the binding energy of the hydrocarbon C 1s feature to 284.8 eV.

Inductively coupled plasma-optical emission spectroscopy (ICP-OES) was used to measure the contents of Li, Ni, Co and Mn in NCM83 before and after the treatments.

4.3 Cell assembly and electrochemical testing

The cathode slurry was prepared by mixing NCM83 powders, super P and polyvinylidene fluoride (PVDF) with a ratio of 90 : 5 : 5 by weight in *N*-methylpyrrolidone (NMP). The homogeneously mixed slurry was coated onto pieces of Al foil followed by drying at 80 °C and later at 120 °C for 12 hours in a vacuum oven. Coin cells were assembled in an Ar-filled glove box using a Cellgard 2300 separator, a Li metal anode and LiPF_6 in an EC/DEC/FEC based electrolyte. The active mass loadings of cathode electrodes were between 7.5 and 8.8 mg cm^{-2} . The assembled cells were subjected to galvanostatic charge and discharge at room temperature in a voltage range of 2.8 to 4.25 V vs. Li/Li^+ using a LAND CT2001A battery testing system (Wuhan LAND Electronic Co., Ltd.). The theoretical capacity is 200 mA h g^{-1} . The current density used for charging/discharging at 0.1C is 20 mA g^{-1} .

Electrochemical impedance spectroscopy (EIS) measurements were conducted using a Zahner Zennium electrochemical workstation. Cells were charged to 3.65 V vs. Li/Li^+ before taking the measurement. The frequency range used was 500 kHz to 10 mHz, and the voltage amplitude was 10 mV. Measurements were taken at the 2nd, 30th, 50th and 100th cycle to monitor the change in cell impedance over cycling. The obtained spectra were fitted by using an electrical equivalent circuit using Nova software to differentiate the impedance associated with Li transport and charge transfer processes at the cathode side.

Data availability

All data are available in the main text or the ESI.†

Author contributions

J. Wang, Z. Zhang and F. Wu conceived this project and determined the framework of the article together. J. Wang and Z. Zhang carried out the experiment. J. Wang analyzed the data, and finished this manuscript under the guidance of F. Wu. J. Wang performed literature research and experimental development and optimized image drawing. F. Wu revised the manuscript. W. He contributed to the validation of the experimental results. W. He and Q. Li conducted extra experiments during the manuscript revision process. Z. Zhang and Z. Wang contributed to the analysis of the experiment results. S. Weng obtained the TEM images. All authors discussed and commented on the manuscript. F. Wu supervised the project.

Conflicts of interest

The authors declare that they have no competing interests.

Acknowledgements

This work was supported by the Outstanding Youth Fund Project by the Department of Science and Technology of Jiangsu Province (Grant No. BK20220045), Key R&D Project funded by the Department of Science and Technology of Jiangsu Province (Grant No. BE2020003), Key Program-Automobile Joint Fund of the National Natural Science Foundation of China (Grant No. U1964205), General Program of the National Natural Science Foundation of China (Grant No. 51972334), General Program of the National Natural Science Foundation of Beijing (Grant No. 2202058), Cultivation Project of Leading Innovative Experts in Changzhou City (CQ20210003), National Overseas High-level Expert recruitment Program (Grant No. E1JF021E11), Talent Program of the Chinese Academy of Sciences, “Scientist Studio Program Funding” from the Yangtze River Delta Physics Research Center and Tianmu Lake Institute of Advanced Energy Storage Technologies (Grant No. TIES-SS0001) and Science and Technology Research Institute of the China Three Gorges Corporation (Grant No. 202103402). The authors also thank Dr Yapei Li at Huairou Division, Institute of Physics, Chinese Academy of Sciences, for fruitful discussion on XRD refinement.

References

- 1 S. T. Myung, *et al.*, Nickel-Rich Layered Cathode Materials for Automotive Lithium-Ion Batteries: Achievements and Perspectives, *ACS Energy Lett.*, 2017, 2(1), 196–223.
- 2 N. Nitta, F. Wu, J. T. Lee and G. Yushin, Li-ion battery materials: Present and future, *Mater. Today*, 2015, 18(5), 252–264.
- 3 Y. Wang, *et al.*, Stable Ni-rich layered oxide cathode for sulfide-based all-solid-state lithium battery, *eScience*, 2022, 2(5), 537–545.
- 4 J. Wang, *et al.*, Interfacial and cycle stability of sulfide all-solid-state batteries with Ni-rich layered oxide cathodes, *Nano Energy*, 2022, 100, 107528.
- 5 K. Min, *et al.*, A comparative study of structural changes in lithium nickel cobalt manganese oxide as a function of Ni content during delithiation process, *J. Power Sources*, 2016, 315, 111–119.
- 6 L. De Biasi, A. O. Kondrakov, H. Geßwein, T. Brezesinski, P. Hartmann and J. Janek, Between Scylla and Charybdis: Balancing among Structural Stability and Energy Density of Layered NCM Cathode Materials for Advanced Lithium-Ion Batteries, *J. Phys. Chem. C*, 2017, 121(47), 26163–26171.
- 7 S. S. Zhang, Problems and their origins of Ni-rich layered oxide cathode materials, *Energy Storage Mater.*, 2020, 24(July 2019), 247–254.
- 8 K. Kang and G. Ceder, Factors that affect Li mobility in layered lithium transition metal oxides, *Phys. Rev. B: Condens. Matter Mater. Phys.*, 2006, 74(9), 1–7.
- 9 D. P. Abraham, R. D. Twisten, M. Balasubramanian, I. Petrov, J. McBreen and K. Amine, Surface changes on LiNi_{0.8}Co_{0.2}O₂ particles during testing of high-power lithium-ion cells, *Electrochem. Commun.*, 2002, 4(8), 620–625.
- 10 H. Zhang, *et al.*, Rock-Salt Growth-Induced (003) Cracking in a Layered Positive Electrode for Li-Ion Batteries, *ACS Energy Lett.*, 2017, 2(11), 2607–2615.
- 11 T. Hatsukade, A. Schiele, P. Hartmann, T. Brezesinski and J. Janek, Origin of Carbon Dioxide Evolved during Cycling of Nickel-Rich Layered NCM Cathodes, *ACS Appl. Mater. Interfaces*, 2018, 10(45), 38892–38899.
- 12 N. Mahne, S. E. Renfrew, B. D. McCloskey and S. A. Freunberger, Electrochemical Oxidation of Lithium Carbonate Generates Singlet Oxygen, *Angew. Chem., Int. Ed.*, 2018, 57(19), 5529–5533.
- 13 G. V. Zhuang, G. Chen, J. Shim, X. Song, P. N. Ross and T. J. Richardson, Li₂CO₃ in LiNi_{0.8}Co_{0.15}Al_{0.05}O₂ cathodes and its effects on capacity and power, *J. Power Sources*, 2004, 134(2), 293–297.
- 14 R. Jung, *et al.*, Effect of Ambient Storage on the Degradation of Ni-Rich Positive Electrode Materials (NMC811) for Li-Ion Batteries, *J. Electrochem. Soc.*, 2018, 165(2), A132–A141.
- 15 N. V. Faenza, *et al.*, Editors' Choice—Growth of Ambient Induced Surface Impurity Species on Layered Positive Electrode Materials and Impact on Electrochemical Performance, *J. Electrochem. Soc.*, 2017, 164(14), A3727–A3741.
- 16 J. Sicklinger, M. Metzger, H. Beyer, D. Pritzl and H. A. Gasteiger, Ambient Storage Derived Surface Contamination of NCM811 and NCM111: Performance Implications and Mitigation Strategies, *J. Electrochem. Soc.*, 2019, 166(12), A2322–A2335.
- 17 K. Shizuka, C. Kiyohara, K. Shima and Y. Takeda, Effect of CO₂ on layered Li_{1+z}Ni_{1-x-y}CoxMyO₂ (M = Al, Mn) cathode materials for lithium ion batteries, *J. Power Sources*, 2007, 166(1), 233–238.
- 18 X. J. Zhu, H. H. Chen, H. Zhan, D. L. Yang and Y. H. Zhou, Storage characteristics of LiNi_{0.85}Co_{0.15}O₂ in air as cathode material for lithium-ion batteries, *J. Mater. Sci.*, 2005, 40(11), 2995–2997.
- 19 H. S. Liu, Z. R. Zhang, Z. L. Gong and Y. Yang, Origin of deterioration for LiNiO₂ cathode material during storage in air, *Electrochem. Solid-State Lett.*, 2004, 7(7), A190.
- 20 H. Liu, Y. Yang and J. Zhang, Investigation and improvement on the storage property of LiNi_{0.8}Co_{0.2}O₂ as a cathode material for lithium-ion batteries, *J. Power Sources*, 2006, 162(1), 644–650.
- 21 A. Van der Ven and G. Ceder, Lithium diffusion mechanisms in layered intercalation compounds, *J. Power Sources*, 2001, 97–98(December 2000), 529–531.
- 22 M. D. Radin, *et al.*, Narrowing the Gap between Theoretical and Practical Capacities in Li-Ion Layered Oxide Cathode Materials, *Adv. Energy Mater.*, 2017, 7(20), 1–33.
- 23 S. H. Kang, W. S. Yoon, K. W. Nam, X. Q. Yang and D. P. Abraham, Investigating the first-cycle irreversibility of lithium metal oxide cathodes for Li batteries, *J. Mater. Sci.*, 2008, 43(14), 4701–4706.

- 24 A. Liu, *et al.*, Factors that Affect Capacity in the Low Voltage Kinetic Hindrance Region of Ni-Rich Positive Electrode Materials and Diffusion Measurements from a Reinvented Approach, *J. Electrochem. Soc.*, 2021, **168**(7), 070503.
- 25 R. Robert, C. Bunzli, E. J. Berg and P. Novák, Activation Mechanism of $\text{LiNi}_0.80\text{Co}_0.15\text{Al}_0.05\text{O}_2$: Surface and bulk operando electrochemical, differential electrochemical mass spectrometry, and x-ray diffraction analyses, *Chem. Mater.*, 2015, **27**(2), 526–536.
- 26 A. O. Kondrakov, *et al.*, Anisotropic Lattice Strain and Mechanical Degradation of High- and Low-Nickel NCM Cathode Materials for Li-Ion Batteries, *J. Phys. Chem. C*, 2017, **121**(6), 3286–3294.
- 27 J. Li, J. Harlow, N. Stakheiko, N. Zhang, J. Paulsen and J. Dahn, Dependence of Cell Failure on Cut-Off Voltage Ranges and Observation of Kinetic Hindrance in $\text{LiNi}_0.8\text{Co}_0.15\text{Al}_0.05\text{O}_2$, *J. Electrochem. Soc.*, 2018, **165**(11), A2682–A2695.
- 28 X. Zheng, *et al.*, Investigation and improvement on the electrochemical performance and storage characteristics of LiNiO_2 -based materials for lithium ion battery, *Electrochim. Acta*, 2016, **191**, 832–840.
- 29 L. You, B. Chu, G. Li, Tao Huang and Aishui Yu, H_3BO_3 washed $\text{LiNi}_0.8\text{Co}_0.1\text{Mn}_0.1\text{O}_2$ with enhanced electrochemical performance and storage characteristics, *J. Power Sources*, 2021, **482**, 228940.
- 30 W. Lee, *et al.*, Destabilization of the surface structure of Ni-rich layered materials by water-washing process, *Energy Storage Mater.*, 2022, **44**(October 2021), 441–451.
- 31 D. Pritzl, *et al.*, Editors' Choice—Washing of Nickel-Rich Cathode Materials for Lithium-Ion Batteries: Towards a Mechanistic Understanding, *J. Electrochem. Soc.*, 2019, **166**(16), A4056–A4066.
- 32 X. Xiong, *et al.*, Washing effects on electrochemical performance and storage characteristics of $\text{LiNi}_0.8\text{Co}_0.1\text{Mn}_0.1\text{O}_2$ as cathode material for lithium-ion batteries, *J. Power Sources*, 2013, **222**, 318–325.
- 33 J. Kim, Y. Hong, K. S. Ryu, M. G. Kim and J. Cho, Washing effect of a $\text{LiNi}_0.83\text{Co}_0.15\text{Al}_0.02\text{O}_2$ cathode in water, *Electrochem. Solid-State Lett.*, 2006, **9**(1), 5.
- 34 K. Park, *et al.*, Re-construction layer effect of $\text{LiNi}_0.8\text{Co}_0.15\text{Mn}_0.05\text{O}_2$ with solvent evaporation process, *Sci. Rep.*, 2017, **7**(March), 1–10.
- 35 M. Bianchini, M. Roca-Ayats, P. Hartmann, T. Brezesinski and J. Janek, There and back again—the journey of LiNiO_2 as a cathode active material, *Angew. Chem., Int. Ed.*, 2019, **58**(31), 10434–10458.
- 36 R. Moshitev, P. Zlatilova, S. Vasilev, I. Bakalova and A. Kozawa, Synthesis, XRD characterization and electrochemical performance of overlithiated LiNiO_2 , *J. Power Sources*, 1999, **81**(82), 434–441.
- 37 R. Moshitev, P. Zlatilova, V. Manev and K. Tagawa, Synthesis of LiNiO_2 in air atmosphere: X-ray diffraction characterization and electrochemical investigation, *J. Power Sources*, 1996, **62**(1), 59–66.
- 38 H. L. Andersen, E. A. Cheung, M. Avdeev, H. E. Maynard-Casely, D. P. Abraham and N. Sharma, Consequences of long-term water exposure for bulk crystal structure and surface composition/chemistry of nickel-rich layered oxide materials for Li-ion batteries, *J. Power Sources*, 2020, **470**, 228370.
- 39 E. Flores, N. Vonnrüti, P. Novák, U. Aschauer and E. J. Berg, Elucidation of $\text{Li}_x\text{Ni}_{0.8}\text{Co}_{0.15}\text{Al}_{0.05}\text{O}_2$ Redox Chemistry by Operando Raman Spectroscopy, *Chem. Mater.*, 2018, **30**(14), 4694–4703.
- 40 Z. Tang, *et al.*, Facilitating Lithium-Ion Diffusion in Layered Cathode Materials by Introducing Li⁺/Ni²⁺ Antisite Defects for High-Rate Li-Ion Batteries, *Research*, 2019, **2019**, 1–10.
- 41 S. E. Renfrew and B. D. McCloskey, Quantification of Surface Oxygen Depletion and Solid Carbonate Evolution on the First Cycle of $\text{LiNi}_{0.6}\text{Mn}_{0.2}\text{Co}_{0.2}\text{O}_2$ Electrodes, *ACS Appl. Energy Mater.*, 2019, **2**, 3762–3772.
- 42 S. E. Renfrew, L. A. Kaufman and B. D. McCloskey, Altering Surface Contaminants and Defects Influences the First-Cycle Outgassing and Irreversible Transformations of $\text{LiNi}_{0.6}\text{Mn}_{0.2}\text{Co}_{0.2}\text{O}_2$, *ACS Appl. Mater. Interfaces*, 2019, **11**(38), 34913–34921.
- 43 S. E. Renfrew and B. D. McCloskey, Residual Lithium Carbonate Predominantly Accounts for First Cycle CO_2 and CO Outgassing of Li-Stoichiometric and Li-Rich Layered Transition-Metal Oxides, *J. Am. Chem. Soc.*, 2017, **139**(49), 17853–17860.
- 44 D.-H. Cho, *et al.*, Effect of Residual Lithium Compounds on Layer Ni-Rich $\text{Li}[\text{Ni}_{0.7}\text{Mn}_{0.3}]\text{O}_2$, *J. Electrochem. Soc.*, 2014, **161**(6), A920–A926.
- 45 S. Koide, Electrical Properties of $\text{Li}_x\text{Ni}_{1-x}\text{O}$ Single Crystals, *J. Phys. Soc. Jpn.*, 1965, **20**(1), 123–132.
- 46 M. D. Levi, K. Gamolsky, D. Aurbach, U. Heider and R. Oesten, On electrochemical impedance measurements of $\text{Li}_x\text{Co}_{0.2}\text{Ni}_{0.8}\text{O}_2$ and Li_xNiO_2 intercalation electrodes, *Electrochim. Acta*, 2000, **45**(11), 1781–1789.
- 47 U. Westerhoff, K. Kurbach, F. Lienesch and M. Kurrat, Analysis of Lithium-Ion Battery Models Based on Electrochemical Impedance Spectroscopy, *Energy Technol.*, 2016, **4**(12), 1620–1630.
- 48 R. Koerver, I. Aygün, T. Leichtweiß, C. Dietrich, W. Zhang, J. O. Binder and J. Janek, Capacity fade in solid-state batteries: interphase formation and chemomechanical processes in nickel-rich layered oxide cathodes and lithium thiophosphate solid electrolytes, *Chem. Mater.*, 2017, **29**(13), 5574–5582.
- 49 D. P. Abraham, S. Kawauchi and D. W. Dees, Modeling the impedance versus voltage characteristics of $\text{LiNi}_{0.8}\text{Co}_{0.15}\text{Al}_{0.05}\text{O}_2$, *Electrochim. Acta*, 2008, **53**(5), 2121–2129.
- 50 S. Contarini and J. W. Rabalais, Ion bombardment-induced decomposition of Li and Ba sulfates and carbonates studied by X-ray photoelectron spectroscopy, *J. Electron Spectrosc. Relat. Phenom.*, 1985, **35**(2), 191–201.
- 51 J. P. Contour, A. Salesse, M. Froment, M. Garreau, J. Thevenin and D. Warin, Analysis by electron-microscopy and XPS of lithium surfaces polarized in anhydrous organic electrolytes, *J. Microsc. Spectrosc. Electron.*, 1979, **4**(4), 483–491.

- 52 Z. Fu, J. Hu, W. Hu, S. Yang and Y. Luo, Quantitative analysis of Ni²⁺/Ni³⁺ in Li [Ni_xMn_yCo_z] O₂ cathode materials: Non-linear least-squares fitting of XPS spectra, *Appl. Surf. Sci.*, 2018, **441**, 1048–1056.
- 53 A. W. Moses, H. G. G. Flores, J. G. Kim and M. A. Langell, Surface properties of LiCoO₂, LiNiO₂ and LiNi_{1-x}Co_xO₂, *Appl. Surf. Sci.*, 2007, **253**(10), 4782–4791.
- 54 M. Oku, H. Tokuda and K. Hirokawa, Final states after Ni_{2p} photoemission in the nickel–oxygen system, *J. Electron Spectrosc. Relat. Phenom.*, 1991, **53**(4), 201–211.
- 55 S. Deng, *et al.*, Insight into cathode surface to boost the performance of solid-state batteries, *Energy Storage Mater.*, 2021, **35**(December 2020), 661–668.
- 56 T. Wei, P. Peng, Y. Ji, Y. Zhu, T. Yi and Y. Xie, Rational construction and decoration of Li₅Cr₇Ti₆O₂₅@C nanofibers as stable lithium storage materials, *J. Energy Chem.*, 2022, **71**, 400–410.
- 57 Y. Bi, *et al.*, Correlation of oxygen non-stoichiometry to the instabilities and electrochemical performance of LiNi_{0.8}Co_{0.1}Mn_{0.1}O₂ utilized in lithium ion battery, *J. Power Sources*, 2015, **283**, 211–218.
- 58 R. T. Haasch and D. P. Abraham, Lithium-based transition-metal oxides for battery electrodes analyzed by x-ray photoelectron spectroscopy. I. LiNi_{0.8}Co_{0.15}Al_{0.05}O₂, *Surf. Sci. Spectra*, 2019, **26**(1), 014003.
- 59 K. Zhou, *et al.*, Identical cut-off voltage: Versus equivalent capacity: An objective evaluation of the impact of dopants in layered oxide cathodes, *J. Mater. Chem. A*, 2021, **9**(18), 11219–11227.
- 60 S. Tanaka, M. Taniguchi and H. Tanigawa, XPS and UPS studies on electronic structure of Li₂O, *J. Nucl. Mater.*, 2000, **283–287**(PART II), 1405–1408.
- 61 K. S. Park, S. H. Park, Y. K. Sun, K. S. Nahm, Y. S. Lee and M. Yoshio, Effect of oxygen flow rate on the structural and electrochemical properties of lithium nickel oxides synthesized by the sol-gel method, *J. Appl. Electrochem.*, 2002, **32**(11), 1229–1233.
- 62 F. Kong, C. Liang, L. Wang, Y. Zheng, S. Peranathan, R. C. Longo and K. Cho, Kinetic stability of bulk LiNiO₂ and surface degradation by oxygen evolution in LiNiO₂-based cathode materials, *Adv. Energy Mater.*, 2019, **9**(2), 1802586.
- 63 T. Sata, High-temperature vaporization of Li₂O component from solid solution Li_xNi_{1-x}O in air, *Ceram. Int.*, 1998, **24**(1), 53–59.
- 64 E. McCalla, G. H. Carey and J. R. Dahn, Lithium loss mechanisms during synthesis of layered Li_xNi_{2-x}O₂ for lithium ion batteries, *Solid State Ionics*, 2012, **219**, 11–19.
- 65 H. X. Yang, Q. F. Dong, X. H. Hu, X. P. Ai and S. X. Li, Preparation and characterization of LiNiO₂ synthesized from Ni(OH)₂ and LiOH·H₂O, *J. Power Sources*, 1999, **79**(2), 256–261.
- 66 T. S. Horányi, The thermal stability of the β-Ni(OH)₂-β NiOOH system, *Thermochim. Acta*, 1989, **137**(2), 247–253.
- 67 J.-G. Kim, D. L. Pugmire, D. Battaglia and M. A. Langell, Analysis of the NiCo₂O₄ spinel surface with Auger and X-ray photoelectron spectroscopy, *Appl. Surf. Sci.*, 2000, **165**(1), 70–84.
- 68 S. A. Chambers, Epitaxial growth and properties of thin film oxides, *Surf. Sci. Rep.*, 2000, **39**(5–6), 105–180.
- 69 M. A. Langell, J. G. Kim, D. L. Pugmire and W. McCarroll, Nature of oxygen at rocksalt and spinel oxide surfaces, *J. Vac. Sci. Technol., A*, 2001, **19**(4), 1977–1982.
- 70 M. A. Langell, M. D. Anderson, G. A. Carson, L. Peng and S. Smith, Valence-band electronic structure of Co₃O₄ epitaxy on CoO (100), *Phys. Rev. B: Condens. Matter Mater. Phys.*, 1999, **59**(7), 4791.
- 71 L. Zou, *et al.*, Unlocking the passivation nature of the cathode–air interfacial reactions in lithium ion batteries, *Nature communications*, 2020, **11**(1), 3204.
- 72 M. C. Biesinger, B. P. Payne, A. P. Grosvenor, L. W. M. Lau, A. R. Gerson and R. S. C. Smart, Resolving surface chemical states in XPS analysis of first row transition metals, oxides and hydroxides: Cr, Mn, Fe, Co and Ni, *Appl. Surf. Sci.*, 2011, **257**(7), 2717–2730.
- 73 T. F. Yi, L. Y. Qiu, J. Mei, S. Y. Qi, P. Cui, S. Luo and Y. B. He, Porous spherical NiO@NiMoO₄@PPy nanoarchitectures as advanced electrochemical pseudocapacitor materials, *Sci. Bull.*, 2020, **65**(7), 546–556.
- 74 K. S. Kim and N. Winograd, X-ray photoelectron spectroscopic studies of nickel-oxygen surfaces using oxygen and argon ion-bombardment, *Surf. Sci.*, 1974, **43**(2), 625–643.
- 75 T. F. Yi, L. Shi, X. Han, F. Wang, Y. Zhu and Y. Xie, Approaching high-performance lithium storage materials by constructing hierarchical CoNiO₂@CeO₂ nanosheets, *Energy Environ. Mater.*, 2021, **4**(4), 586–595.
- 76 W. S. Yoon, K. Y. Chung, J. McBreen and X. Q. Yang, A comparative study on structural changes of LiCo_{1/3}Ni_{1/3}Mn_{1/3}O₂ and LiNi_{0.8}Co_{0.15}Al_{0.05}O₂ during first charge using in situ XRD, *Electrochem. Commun.*, 2006, **8**(8), 1257–1262.